2013

Development and Validation of an Absorption Sensor for Time-Resolved Measurements of CO and CO2

Kyle Thurmond
University of Central Florida

DEVELOPMENT AND VALIDATION OF AN ABSORPTION SENSOR FOR TIME-RESOLVED MEASUREMENTS OF CO AND CO2

by

KYLE D. THURMOND

A thesis submitted in partial fulfillment of the requirements
for the Honors in the Major Program in Mechanical Engineering
in the College of Engineering and Computer Science
and in The Burnett Honors College
at the University of Central Florida
Orlando, Florida

Fall Term 2013

Thesis Chair: Dr. Subith S. Vasu

ABSTRACT

A sensor was developed for simultaneous measurements of carbon monoxide and carbon dioxide fluctuations in internal combustion engine exhaust gases. This sensor utilizes low-cost and compact LEDs that emit in the 3-5μm wavelength range which are more appropriate for practical applications than the more traditionally used lasers. An affordable, fast response sensor that can measure these gases has broad application that can lead to more efficient, fuel flexible engines and regulations of harmful emissions. LEDs have a more spectrally broad and diverging emission than lasers which presented many design challenges. The optical design software ZEMAX was utilized to overcome these challenges. CO and CO2 LED measurements are conducted in their fundamental bands centered at 4.7μm and 4.3μm, respectively, while a reference LED at 3.6μm is used as a reference for H2O. Tests were carried out using a simple flow cell for validation and calibration of the instrument. The sensor was able to see 0.1% changes in CO_2 and about 0.3% changes CO. No interference between CO and CO_2 was observed.

ACKNOWLEDGMENTS

Research at UCF was supported by financial assistance from Duke Energy (formerly Progress Energy Florida), the UCF Mechanical and Aerospace Department, and the UCF Office of Research and Commercialization. This research would not have been possible without the support and encouragement during difficult times from Dr. Subith Vasu. Additionally, collaboration with Dr. Bill Partridge and Dr. Maggie Connatser from Oak Ridge National Laboratory was vital to the success of this work. The Oak Ridge National Laboratory work is sponsored by the U.S. Department of Energy, Office of Energy Efficiency and Renewable Energy, Vehicle Technologies Program.

TABLE OF CONTENTS

LIST OF FIGURES

LIST OF TABLES

CHAPTER 1: INTRODUCTION

Motivation

There is a crucial need to reduce the amount of fossils fuels used in order to mitigate dependencies on foreign oil, the effects of global climate change, and risks to public health. However, liquid fuel consumption is projected to increase by 38% from 2010 to 2040 with the transportation sector accounting for 63% of that increase [1]. There is not a single solution to these far-reaching issues and part of an overall solution will be moving from fossil fuels to biologically based liquid fuels that can have net zero carbon cycle while simultaneously improving combustion efficacies [2]. The development of sensors that are capable of detecting exhaust gases can assist in the advancement of adaptive engines that are fuel flexible with increased efficiency.

A sensor that can simultaneously monitor Carbon Monoxide (CO) and Carbon Dioxide (CO_2) will have benefits in emissions control and combustion control applications. CO is a primary product of incomplete combustion which can be used to indicate combustion efficiency. CO is also toxic to humans and animals, so is regulated by the U.S. Environmental Protection Agency. Regulations require Continues Emissions Monitory (CEM) in stationary sources that emit, or have the potential to emit, CO, including hazardous waste incinerators, boilers, and furnaces. CO_2 represents complete combustion, is a critical greenhouse gas, and, along with CO, is a measure of total exhaust carbon output. Greenhouse gases (GHG) increase the global average temperature by absorbing and emitting thermal radiation that would have otherwise escaped earth's atmosphere. The Intergovernmental Panel on Climate Change (IPCC) fifth assessment on climate change, released 2013, strengthened their degree of certainty that human

activities are responsible for global climate change, reporting that is “extremely likely” (95 to 100% probability) [3]. The changes are resulting in atmosphere and ocean warming, diminished snow and ice, higher and higher sea levels. Additionally, the total carbon output measure can be used to determine fuel input or in monitoring for future carbon regulations.

A sensor that can detect CO_2 in real-time can be used for Exhaust Gas Recirculation (EGR) monitoring and control. This is a well-established technique in reducing nitrogen oxides (NOx) formed at high temperatures in combustion engines. External EGR works by recirculating a portion of the exhaust gases back into the engine. Whereas in internal EGR the residual burned gas remains in the cylinder from the previous cycle, which makes it more difficult monitor. The effect of this technique is a reduction in flame temperatures by increasing the heat capacity of the inlet charge without altering the air to fuel ratio which can also benefit fuel economy. Poor EGR control can result in excessive quenching of the mixture leading to poor combustion quality and may increase difficulties to burn smoke free [4].

Further, this sensor can be used in the development of new advanced engines that have lower emissions and operability with alternative fuels (e.g. biofuels). The adoption of alternative fuels is necessary to reduce or eliminate foreign oil dependencies. Engines will need to be able operate on both fossil fuels and newer fuels in order for a transition to occur, however combustion efficiency is highly dependent on fuel chemistry [5]. A sensor that can detect exhaust gas species can be used for closed-looped control in development of fuel flexible engines. The application of these concepts aren’t limited to automotive engines; such a sensor

can have broad application in stationary gas turbines as well for which performance is highly dependent on gas chemistry [6].

Laser Absorption Spectroscopy and Light Emitting Diodes

Laser based measurement strategies have been developed extensively in combustion and propulsion related research due to its ability to non-intrusively produce quick time-resolved measurements of gas composition, temperature, velocity, and pressure [7-12]. Absorption spectroscopy can target a molecular species by its characteristic absorption spectrum. In species concentration measurement, a collimated beam of light with a wavelength characteristic to the targeted species is directed through a gas. The attenuation of the beam is measured by comparing the incident and transmitted radiation, which is related to molecular concentration.

Lasers are traditionally used in application of this technique which has limited it to laboratory and industrial settings due to cost and complexity. Light-emitting diodes (LED) present a solution for the development of a sensor that is cost effective and rugged enough for practical implementation in automobiles. Partridge et al. have shown the advantages and practicality of such a sensor by developing diagnostics for resolving CO_2 fluctuations with mid-infrared (MIR) LEDs [13, 14]. An LED based sensor, as described here, can be used to make in situ measurements that are nonintrusive and can provide path-averaged species concentration which can relate overall composition for imperfectly mixed flows. The sensor can also be coupled with a probe allowing for both temporal and spatial resolved measurements which may be useful in diagnosing non-uniformities in exhaust flow. A single-point access type probe would

also allow for measurement in areas where two-point access is difficult or not possible, such as in internal EGR and integrated intake runners.

Using LEDs is not without its drawbacks, for which they will need to be accounted for and the sensor properly validated. To name a few, LEDs are spectrally broad, are not as intense as lasers, and emit incoherent light. The emitted spectrum of the LEDs span several transitions which create uncertainty associated with interfering species such as water vapor. With lasers a transition can be picked out on the basis of strength and overlap with other species, and then targeted. The LEDs will need to be passed through a filter to narrow the bandwidth however they will remain quite broad and will lose intensity after being transmitted through. In concern for low power output, a cooled detector with high sensitivity is used for measuring the beam attenuation. It is inherently difficult to collimate and focus to a point incoherent light, which is necessary when transmitting through the gases and focusing onto the detector, respectively. To address this, simulation software is used to optimize the lens design setup to achieve the best performance with minimal losses. Noise from interfering species and losses from non-ideal light sources are characterized and appropriate calibration is done for the greatest effectiveness of the sensor.

Literature Review

The following literature was consulted for methodologies, instruments, and selection of absorption spectrum. The literature covers sensors developed using lasers which may be replicated and used for comparison in future work.

The most recent detection of CO has been carried out by Ren et al. using mid-infrared (MIR) distributed-feedback quantum-cascade lasers [7]. This sensor accessed the fundamental

band of CO around 4.6 and 4.8μm which offers absorption strength 10^4 and 10^2 times stronger compared to the overtone bands near 1.55μm and 2.3μm, respectively. Validation of the sensor using both a fixed-wavelength and scanned-wavelength direct absorption strategies was carried out in nonreactive shock-heated gases. Further tests were carried out in a kinetic study of high-temperature pyrolysis of methyl formate (MF) with measurements compared to simulations performed in CHEMKIN-PRO. Fixed-wavelength measurements detected CO concentrations within 1.7% accuracy with a sample rate of 1MHz, which was limited only by the bandwidth of the detector.

A tunable diode-laser (TDL) sensor that measures CO_2 absorption in the near infrared (NIR) around 2.7μm was developed by Farooq et al. [8]. This region has stronger absorption line strengths than the bands near 1.5μm and 2.0μm used previously to sense CO_2 in combustion gases. While performing measurements in a static cell, CO_2 mole fraction was accurately obtained with a standard deviation of 1.6%. The sensor accuracy and response was then validated in shock heated CO_2-Ar mixtures in a shock-tube. Mole fraction measurements were in agreement of the mixture values within 1.5%. The absorption strength of CO_2 in the fundamental band, around 4.7μm, is 60 times greater than that around 2.7μm, which allows for more sensitive sensors. Yet, few studies have been done in this range due to a lack of instrumentation with access to those wavelengths. The few that have been done had limited sampling rates that are insufficient for resolving engine events.

Organization of Thesis

This thesis is organized as follows:

1) Chapter 2 discusses the Beer-Lambert law, the fundamental theory of absorption spectroscopy and diagnostics methods. Central terms and concepts are defined that will be necessary for proceeding chapters. This will review specific strategies used in absorption spectroscopy, how important values were determined, and how this technique can be applied to incoherent sources such as LEDs. Absorption band selection is also discussed.
2) Chapter 3 provides details into the design of the sensor. Component selection and justification is given. LED characteristics and arrangement are discussed. The use of band pass filters and selection is shown. Detector selection and detectability calculations are presented.
3) Chapter 4 will present simulations that were performed to improve the performance of the sensor. The optical simulation software, Zemax, will be discussed and how it was useful in the development of this sensor. Simulations of the pitch are first presented then remaining sensor lens design.
4) Chapter 5 discusses the details and procedure of the validation test carried out. Description of the flow cell used for evaluation is provided and the concentrations of CO and CO_2 used in testing are listed.
5) Chapter 6 presents the results of the sensor evaluation conducted at Oak Ridge National Laboratory. Future work that is planned for more critical evaluation and improving the sensor is also discussed.

CHAPTER 2: THEORY

Beer-Lambert Law

The theory fundamental to determining species concentration through absorption spectroscopy is well known and has been thoroughly discussed in literature [7-12]. Direct absorption spectroscopy follows from the Beer-Lambert law (equation 1) which relates the transmitted intensity I to the incident intensity I_0 when a spectrally narrow radiation at frequency $\nu[\mathrm{cm}^{-1}]$ is directed through a gas medium:

$$\left(\frac{I}{I_0}\right) = \exp(-S\phi P x_i L), \tag{1}$$

Here $S[\mathrm{cm}^{-2}\,\mathrm{atm}^{-1}]$ is the line strength, $\phi[\mathrm{cm}]$ the line-shape function, $P[\mathrm{atm}]$ is the total pressure, $L[\mathrm{cm}]$ the line path length through the gas, and x_i the mole fraction of the absorbing species. The product $k_\nu = S\phi P x_i$ is known as the spectral absorption coefficient. The line strength was generated using the HITRAN 2012 database which provides a compilation of spectroscopic parameters used to predict and simulate the transmission of light in the atmosphere [15].

The line-strength S can be written as a function of temperature as follows:

$$S(T) = S(T_0)\frac{Q(T_0)}{Q(T)}\left(\frac{T_0}{T}\right)\exp\left[-\frac{hcE''}{k}\left(\frac{1}{T}-\frac{1}{T_0}\right)\right]\left[1-\exp\left(\frac{-hc\nu_0}{kT}\right)\right]\left[1-\exp\left(\frac{-hc\nu_0}{kT}\right)\right]^{-1}, \tag{2}$$

where $Q(T)$ is the partition function, $E''[\mathrm{cm}^{-1}]$ the lower-state energy for the transition, $\nu_0[\mathrm{cm}^{-1}]$ the line-center frequency, $T_0[\mathrm{K}]$ the reference temperature where the line-strength is known, h Planck's constant, c speed of light, and k Boltzmann's constant.

Values for the partition function are dependent on the temperature. Here, the partition function was fitted with a cubic polynomial:

$$Q(T) = a + bT + cT^2 + dT^3, \tag{3}$$

where a, b, c, and d are the constants listed below in table 1. This polynomial was fitted to data available in the HITRAN database.

Table 1: Partition function coefficients.

Species	***a***	***b***	***c***	***d***
Water	985.1	691.5	154.2	19.51
CO	3.889	0.3489	-3.83×10^{-6}	3.352×10^{-8}
CO_2	2071	2058	882.4	179.4

The line-shape function ϕ was approximated with a Voigt function for collisional and Doppler broadened transitions. The collision-broadened full-width at half maximum (FWHM) of the absorbing species i is given by

$$\Delta\nu_c = P\sum_j x_j 2\gamma_{ji}, \tag{4}$$

where x_j is the mole fraction of the collisional partner and $2\gamma_{ji}[\mathrm{cm}^{-1}\,\mathrm{atm}^{-1}]$ is the broadening coefficient of j with i. The broadening coefficient $2\gamma_{ij}$ is known at a reference temperature T_0 and scaled as follows:

$$2\gamma(T) = 2\gamma(T_0)\left(\frac{T_0}{T}\right)^n, \tag{5}$$

where n is the temperature coefficient. The air- and self-broadening coefficients were also attained from the HITRAN database. Tests performed to validate the sensor are conducted in air however shock tube experiments are planned which may require investigation of collisional broadening from argon or other gases.

Method of Application

A fixed-wavelength direction absorption method will be used in applications of this sensor, which infers gas concentration directly from Beer's Law (eqn. 1). For this the incident, or baseline, light I_0 must be known which, due to the low cost of LEDs, a separate light source can be used that is known to have no or little interference from expected gases. Using this method, quick measurements can be made with the bandwidth being limited only by the sampling speed of the detector or data acquisition system (DAQ). Since the LEDs are spectrally broad, the total absorption coefficient is determined by integrating the spectral absorption coefficient over the entire spectrum emitted by the filtered LEDs.

Band Selection

The wavelengths that are available using LEDs range from 1.52 to 7μm. Figure 1 on the next page shows the absorption spectrum of CO_2, CO, and H_2O in this range. The largest band for CO_2 is around 4.2μm. CO has the greatest absorption around 4.7μm. H_2O has very little presents in this area. These bands will allow for the greatest resolution using this technique and the strong absorption will help compensate for the low power output of the LEDs.

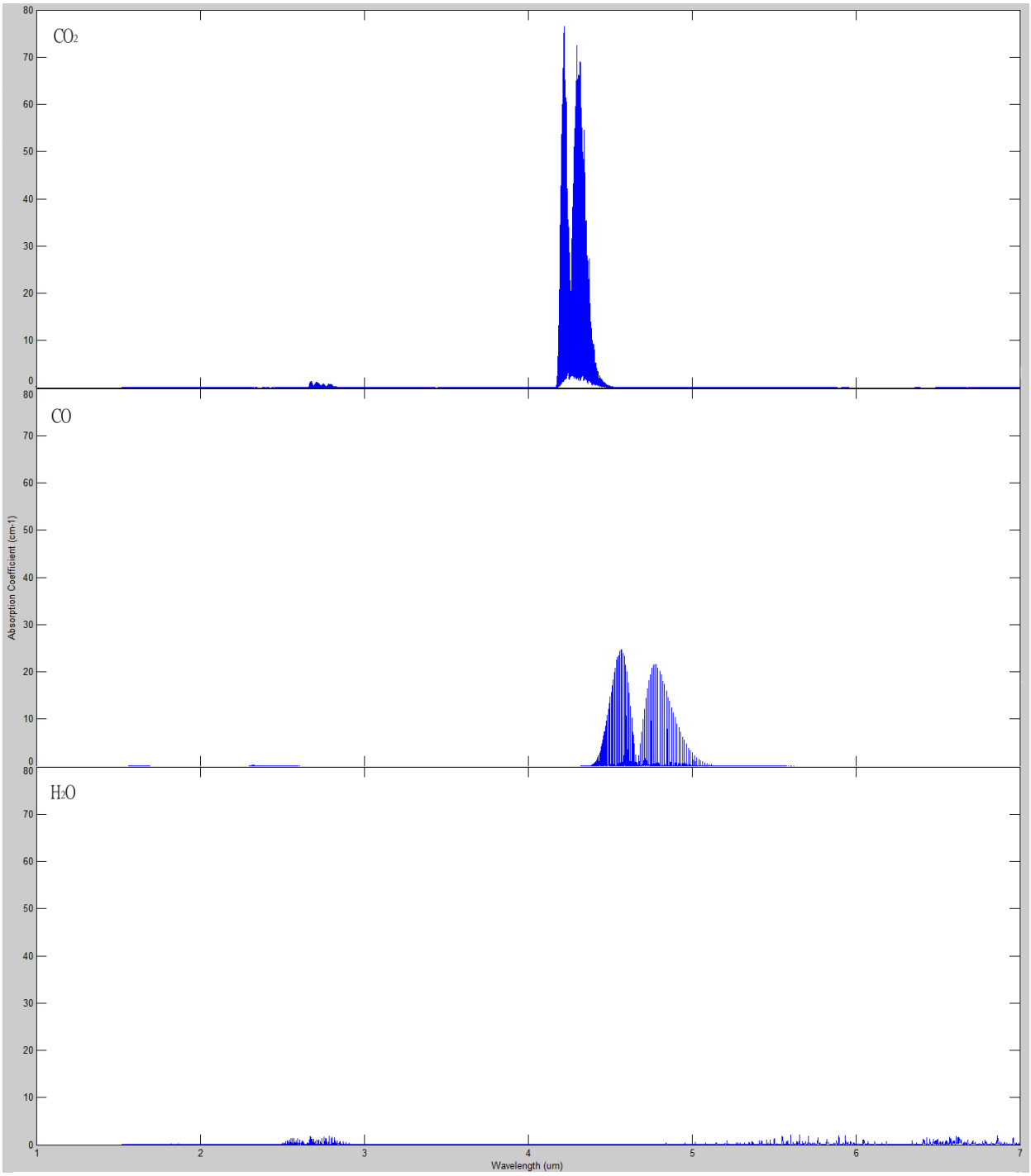

Figure 1: Absorption spectrum for CO2 (top), CO (middle), and H2O (bottom) from 1 to 7um at 800K.

CHAPTER 3: SENSOR DESIGN

Component Selection and Design Details

The basic sensor design architecture is broken down into three major units, the pitch, the catch, and the probe, which is represented in the flowchart in figure 2. In the pitch, three light sources with unique wavelengths is required around 3.6μm for service as a reference (I_0), 4.3μm for detecting CO_2, and 4.7μm for detecting CO. Each LED is to be collimated, filtered, and combined with the other LEDs to form a single light beam. Light guides are to be used to get the signal from the pitch to the probe and from the probe to the catch.

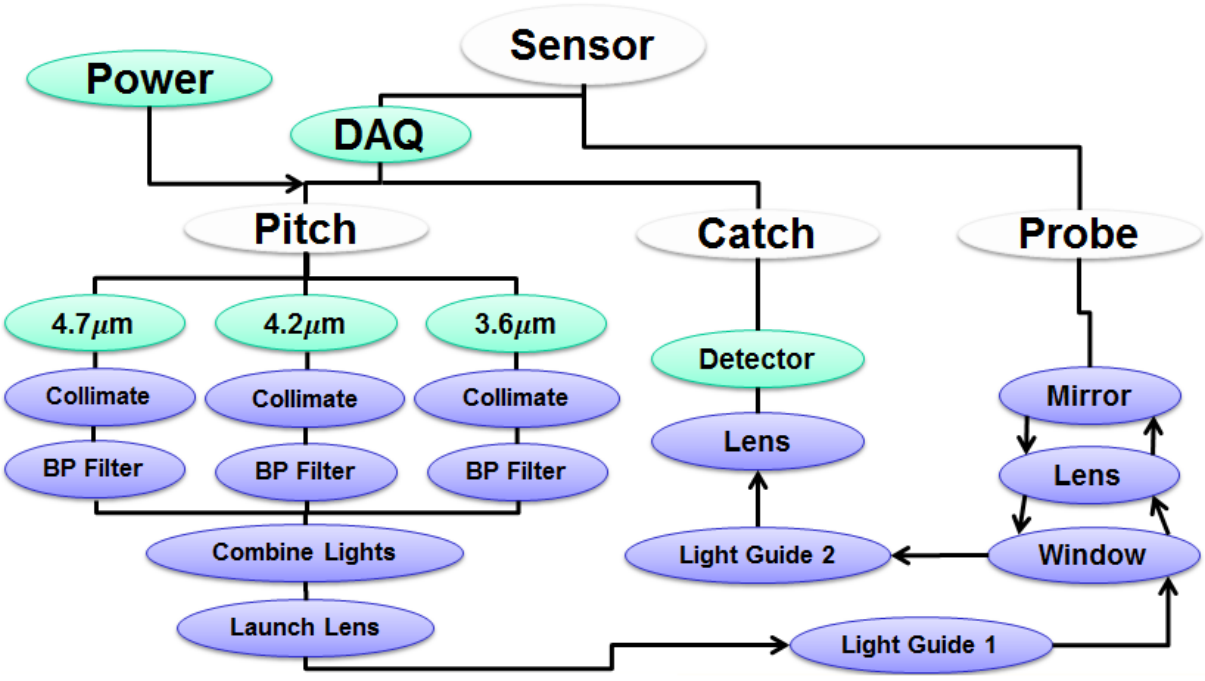

Figure 2: Basic sensor design architecture.

The LED selection criteria were that they emit around the wavelengths previously specified and that they are not highly divergent. The wavelength profiles of the selected LEDs, produced by Ioffe LEDs, are depicted in the figure 3 below as well as the spectral absorption

coefficients for CO, CO_2, and H_2O. The profiles for the LEDs were provided by the manufacturer and are assumed to be accurate. Further specifications for the selected LEDs can be found in the appendix.

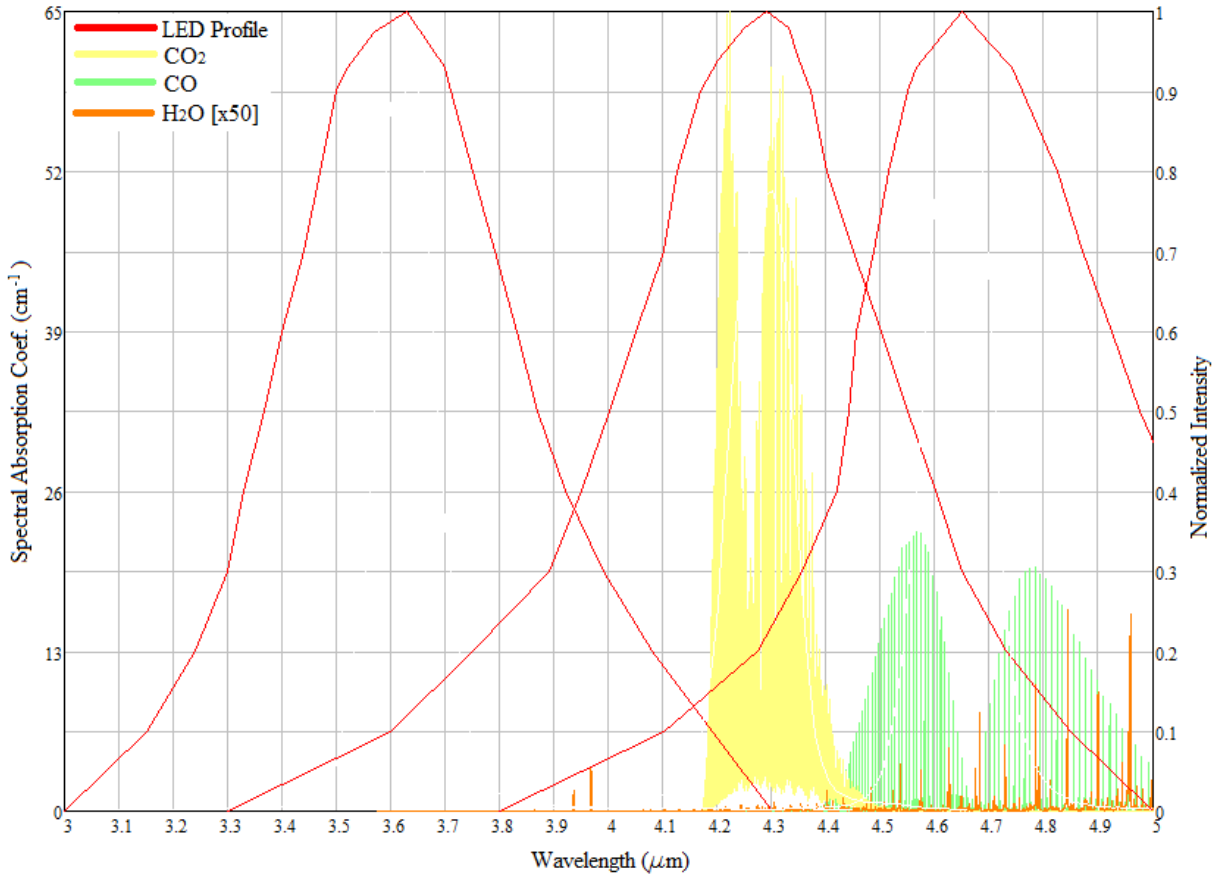

Figure 3: LED spectral profiles and the spectral absorption coefficients for CO, CO_2, and H_2O at 296K.

As previously noted, the spectral emissions of the LEDs are quite broad and significant overlap can be seen. Band pass filters were selected from Edmond Optics that meet the criteria of having a center wavelength over the absorption spectra targeted by each LED, high transmissivity, and minimal or no overlap with other filters. Figure 4 shows the profiles of each LED and respective filters, overlaid on the spectral absorption coefficients of the gases of

interest. These filters have center wavelengths at 3.6μm, 4.26μm, and 4.67μm and transmissivity of 78% or higher. There is small overlap, seen in figure 4, of the CO_2 and CO filters however the transmissivity in this region is below 2% and the absorption strength is relatively small. Additionally, the temperatures of each LED can be controlled so that their center wavelength overlaps with the center wavelength of the corresponding filter so to gain maximum power output. Temperature control is performed using the DAQ.

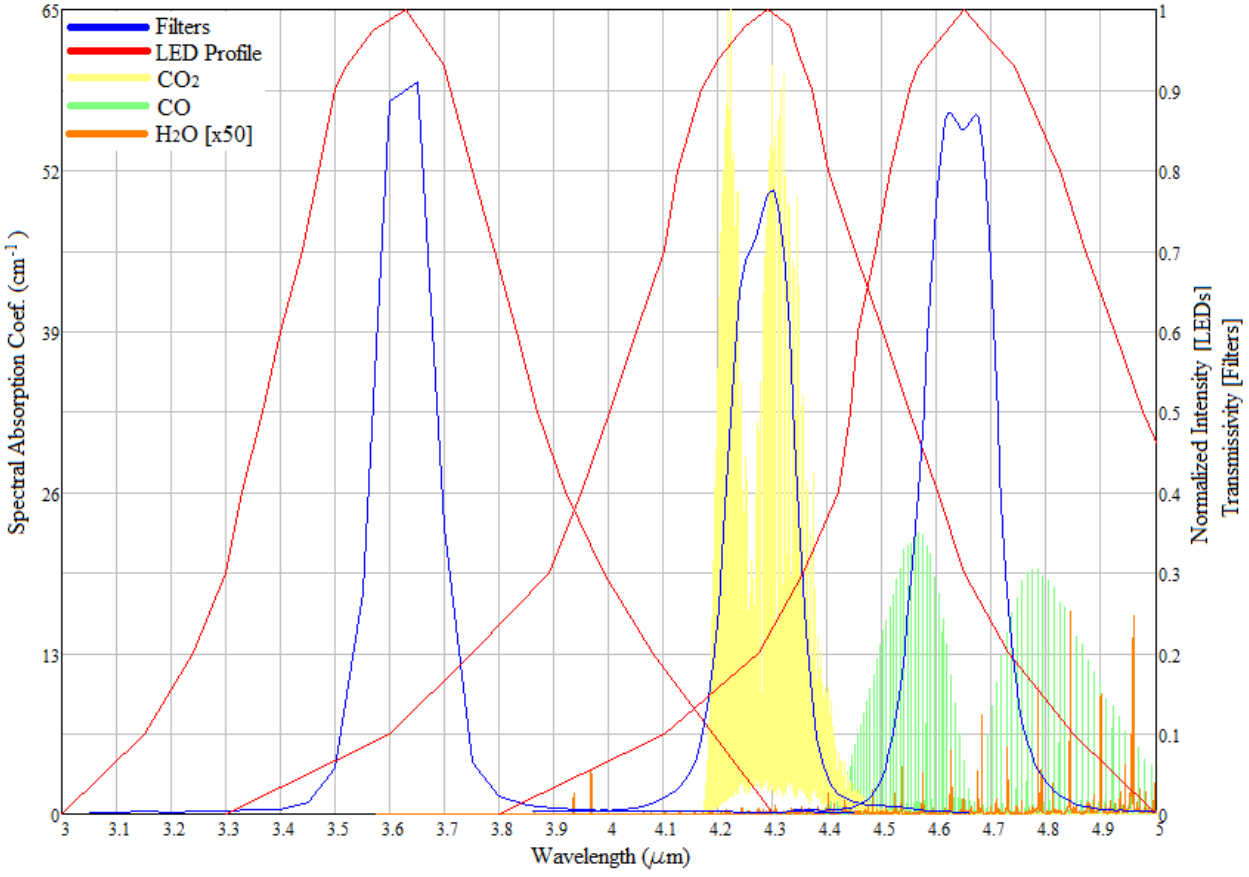

Figure 4: Profiles for LEDs and filters over spectral absorption coefficients.

In order to use only one detector, the LEDs must be collimated and combined into a single beam. A diagram of this and the whole pitch setup are shown below in figure 5. The LED

centered around 4.7μm is significantly less powerful (83 to 96%) than the other LEDs, so a second was placed for compensation. Three Pellicle beam splitters are used to combine the four LEDs. Transmission and reflection for the beam splitters for each center wavelength are shown in table 2. The arrangement of the LEDs and beam splitters was done so to gain the most power output from the 4.7μm LEDs since they are comparatively underpowered. Following the beam splitters, focusing lenses are placed to launch the beam into the hollow silica waveguide (HWG). Selection and placement of lenses will be discussed in the following chapter as this heavily influenced on simulation results.

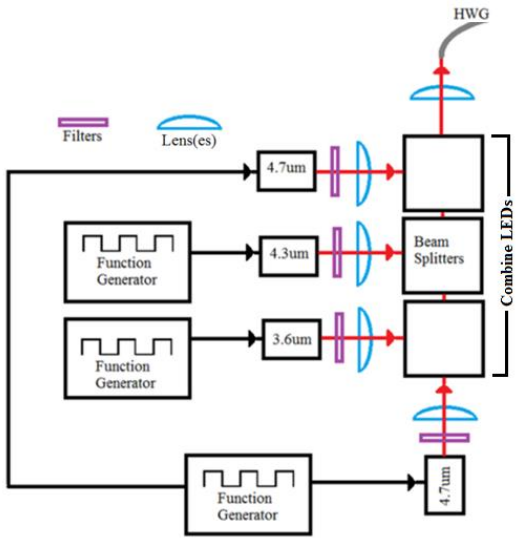

Figure 5: Pitch setup diagram.

Table 2: Pellicle beam splitter transmittance/reflectance.

LED Center Wavelength (μm)	**Reflectance (%)**	**Transmittance (%)**
3.6	33	67
4.2	45	55
4.7	48	53

In figure 2 the probe is represented by a window, lens, and a mirror. This is the basic configuration for a single point access type probe however this sensor is meant to be used with multiple sampling end configurations. Probe, here, will be used as a generalized term denoting a point of access to the gas medium being sampled without exposing it the atmosphere.

The catch is simply the detector and lenses to focus the beam from the light guide into detector. The detector selected is a Vigo Systems three-stage-thermoelectrically-cooled (TEC) photovoltaic detector (model PVI-3TE-5). An STCC-04 TEC controller from the same manufacturer is used detector temperature control. Further specifications for these instruments can be found in appendix. The detectability D^* of the detector is defined as:

$$D^* \equiv \frac{\sqrt{A \times \Delta f}}{NEP} = R_v \frac{\sqrt{A \times \Delta f}}{V_n}, \tag{6}$$

where A is the detector area in cm^2, Δf is the signal bandwidth, V_n is noise voltage, R_v is the voltage responsively of the detector, and NEP is the Noise Equivalent Power [16]. NEP is the optical input power to the detector that produces a signal-to-noise ratio of unity (S/N = 1). For this detector $A = 0.01\mathrm{cm}^2$ and $D^* = 10^{11}$. The optical signal at intermediate frequency due to optical power P and power of radiation of local oscillator P_L is $V_I = R_v(2PP_L)^{1/2}$. NEP is the optical power that generatred the signal equal to noise voltage V_n, so

$$NEP = \frac{V_n^2}{2P_L R_v^2}, \tag{7}$$

Solving for R_v in equation 6 and substituting into equation 7:

$$NEP = \frac{A\Delta f}{2P_L D^{*2}}, \tag{8}$$

The lowest expected LED power output (from the 4.7μm LED) is around 2.5×10^{-7}W. For a bandwidth of 79kHz, $NEP = 1.5 \times 10^{-13}$W. That is an optical power output greater 1.5×10^{-13}W is necessary to be distinguishable from noise, which is sufficient for the selected LEDs.

Criteria for selection of the waveguide are that there is minimal attenuation at the wavelengths being used and that it has the largest inner bore diameter possible. It will be shown in the following chapter on simulations that the majority of the lost power occurs when launching the light into the guides. This is due to the difficulty in focusing to a point the incoherent light of LEDs. For this sensor, a Molex hollow silica waveguide (HWG) is used as it provides the larger inner bore diameter at 1mm. This light guide provides a minimal attenuation of less than 1dB/m for the used wavelengths, as shown in figure 6.

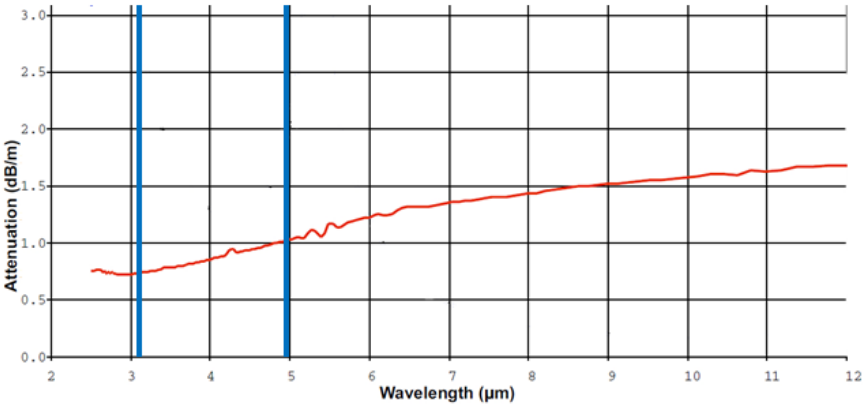

Figure 6: Molex hollow silica waveguide (HWG) attenuation vs. wavelength (μm).

A multi-functional DAQ is used to process the detector signal as well as provide some basic control. The LEDs will be driven by function generators with each unique wavelength being driven at a different frequency so that the signals may be separated using fast Fourier transform (FFT), allowing the use of a single detector. Temperatures of the LEDs are controlled using the DAQ as well. An NI PCI-6259 is used which limits the speed of the sensor to 1MHz.

The entire sensor setup is shown below in figure 7 including the flow cell that is used in evaluation tests. Here a line-of-site access is used where the light is transmitted through the flow cell by windows at each end of the cell.

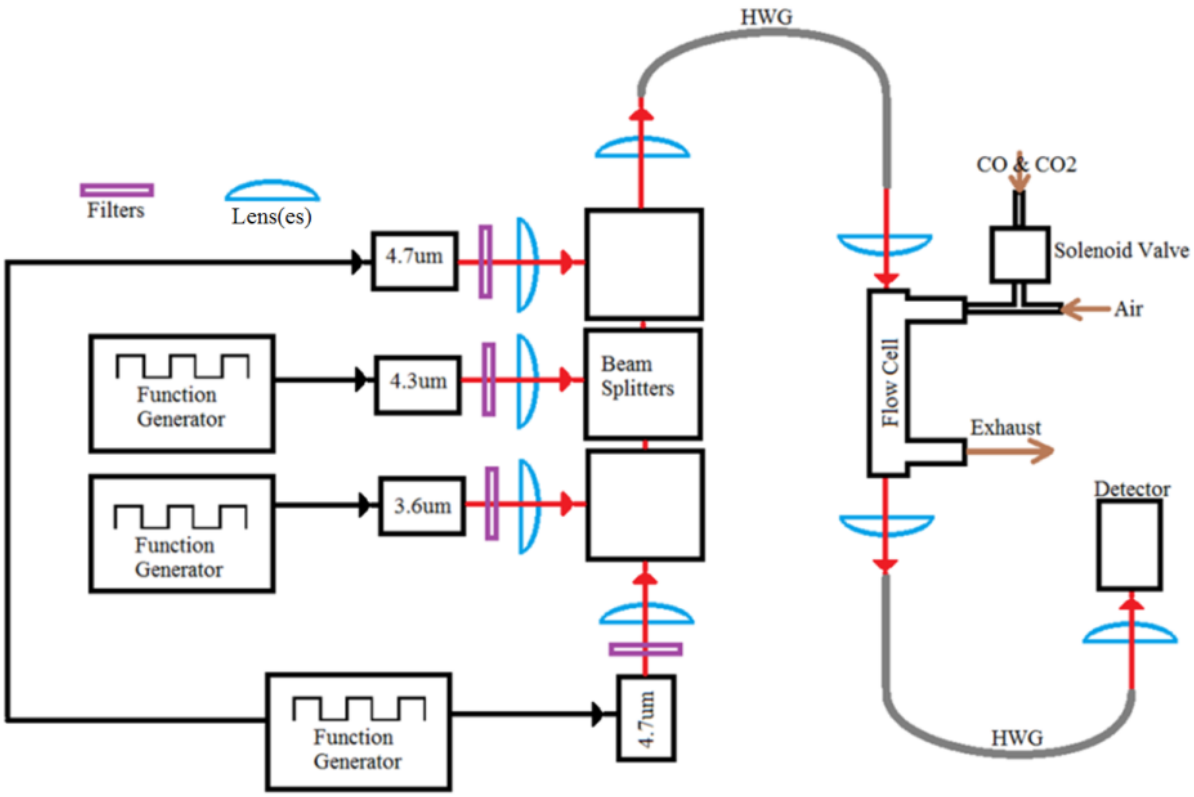

Figure 7: Entire sensor setup including flow cell.

CHAPTER 4: SIMULATIONS

In order to obtain the best performance of the sensor the Radiant Zemax optical-design simulation software was utilized. This software allowed the simulation and optimization of the entire lens design of the sensor. This software is capable of modeling the effects of optical elements ranging from simple lenses and mirrors too diffractive elements, and can produce common analysis diagrams such as spot diagrams and ray-fan plots. Additionally, it can perform standard sequential ray tracing, non-sequential ray tracing for analysis of light scattering, and physical optics beam propagation and has built in optimization capabilities [17].

Pitch Setup Simulations

The sensor utilizes four LEDs which must combine into a single beam. Each LED must be collimated, combined with the other lights, and then launched into the HWG; while each LED has different collimated beam path lengths depending on how many beam splitters it must pass through. This has been a vital part of the designing processes given the inherent difficulties in focusing to a point an incoherent source such as LEDs; a significant amount of power can be loss when attempting to focus the light into the light guide.

Figures below show a one collimating lens, one launch lens setup vs. a two collimating lens/two launch lens for the pitch setup. It is clearly seen that with design 2 a much more collimated beam was achieved, which resulted in less power loss as the light is transmitted through the beam splitters and combined with the other LEDs. The squares here show the incident radiation on the entrance of the HWG. Each square is 6mm by 6mm and display the power density of the incident radiation. Notice that with design 2 the beam was focused to a

smaller, more power dense point. With a 1mm inner bore diameter of the HWG most of our signal is being lost at the entrance of the light guides, so the smaller point is desired. Going from design 1 to design two the efficiency increased at the HWG entrance from 84% to 98%.

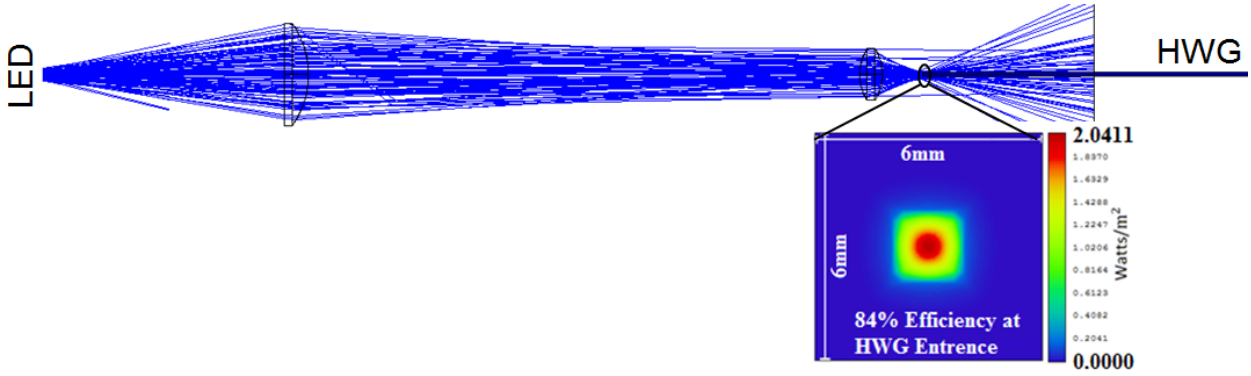

Figure 8: Pitch lens design 1. A one collimating/one launch lens design for the pitch setup.

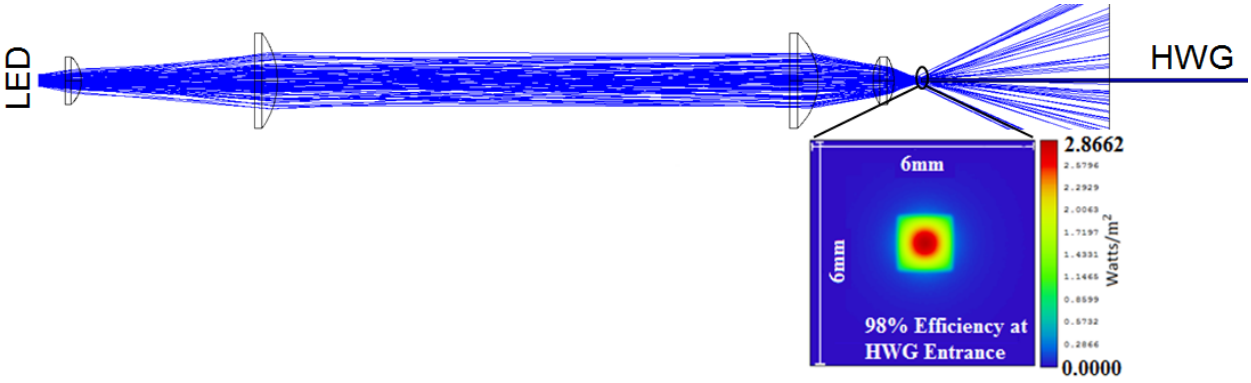

Figure 9: Pitch lens design 2. A two collimating/two launch lens design for the pitch setup.

The following figures show simulations showing the effects of the launch lens focal length. In these simulations all lenses, and distances are the same except for the last launch lens. These simulations use design two from figure 9 above. With the top lens there is a focal length of 15mm and the bottom lens having a very small 5.95mm focal length. The squares shown here are of a detector face approximately 5mm from the exit of the HWG, so it is showing the light after it has been transmitted through the light guide. It is clearly shown that one side effect of the

smaller focal length is an increase numerical aperture which gives the large spot diagram in figure 11. However, there is much less loss achieving an efficiency of 56% with the short focal length versus an efficiency of 40% with the longer focal length at the HWG exit. It should also be pointed out that there is a 98% efficiency at the light guide entrance so half of the signal is lost there, at the entrance.

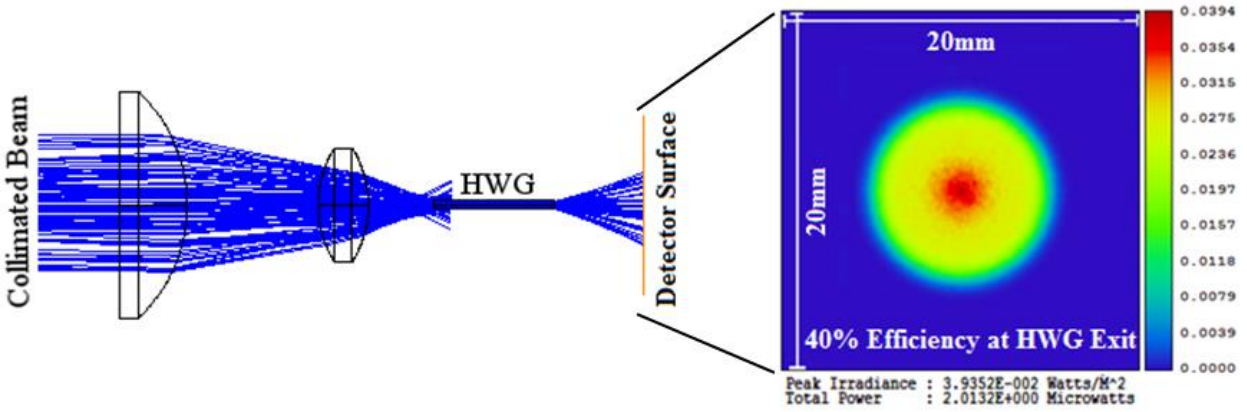

Figure 10: Launch lens simulation with focal length of 15mm.

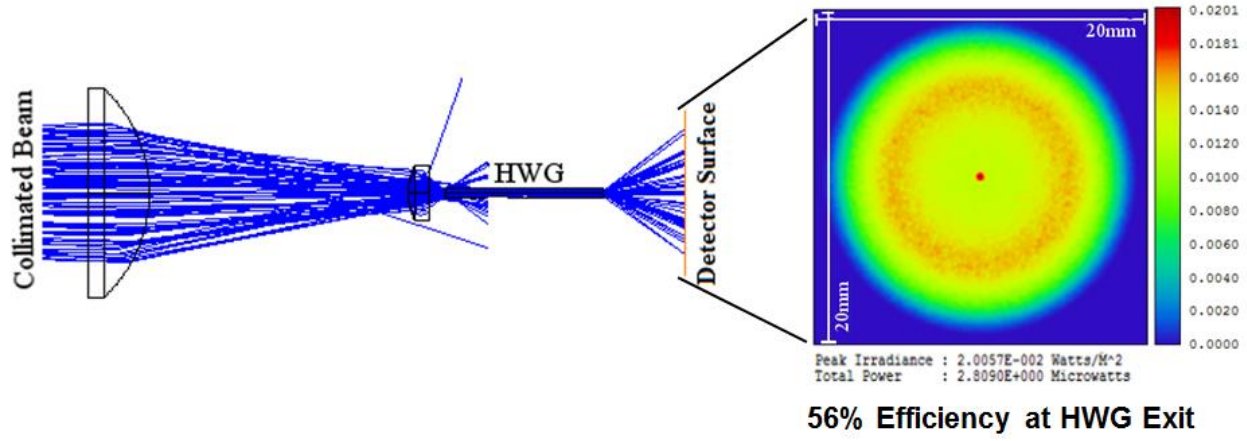

Figure 11: Launch lens simulations with focal length of 5.95mm.

Remaining Sensor Simulations

The above discussion has been limited to the simulation of the pitch setup which took considerably more effort being that it was the most complex lens design of the system. The remaining system simulation is shown below in figure 12. This shows, from right to left, the light exiting the pitch HWG, collimating lenses for the test cell, test cell entrance window aperture, test cell collimated beam path, test cell exit window aperture, catch HWG launch lens, catch HWG, two aspheric focusing lenses for the detector, and finally the detector face. The light exiting the HWG, though having a smaller initial beam diameter, is more divergent than the light that emitted by the LEDs. This is due to the large numerical aperture (NA) from using a short focal length launch lens. This makes it more difficult to re-collimate the beam. The two lines that intersect the beam between the collimating lenses and the launch lenses of the test cell are the profiles of apertures used to simulate the window diameter of the test cells. The beam has a diameter less than this aperture so little or no light was lost here. The distance between these two apertures represents the beam path through the test gases. Again, due to the large NA exiting the HWG, two aspheric lenses had to be used in order to focus the light onto the detector face which is 1mm by 1mm.

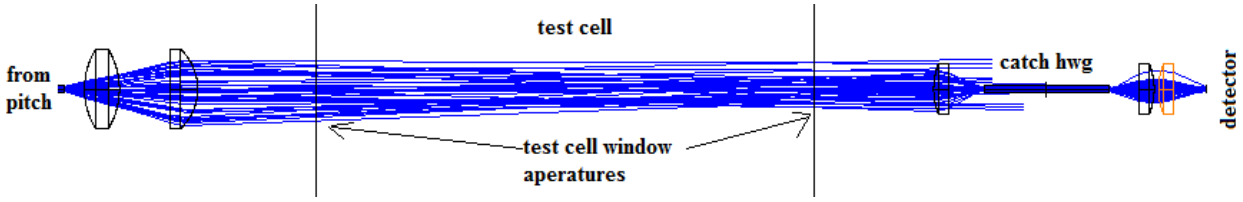

Figure 12: Test cell and catch lens design simulations.

Additionally, a simple lens design was simulated for the purpose of individually evaluating each LED. This consisted of the LED, three lenses, a filter, and the detector. This is

shown in figure 13 below. This set is used to evaluate the losses due to the filter, beam splitters, from light scatter, and from beam waste when launching into HWGs.

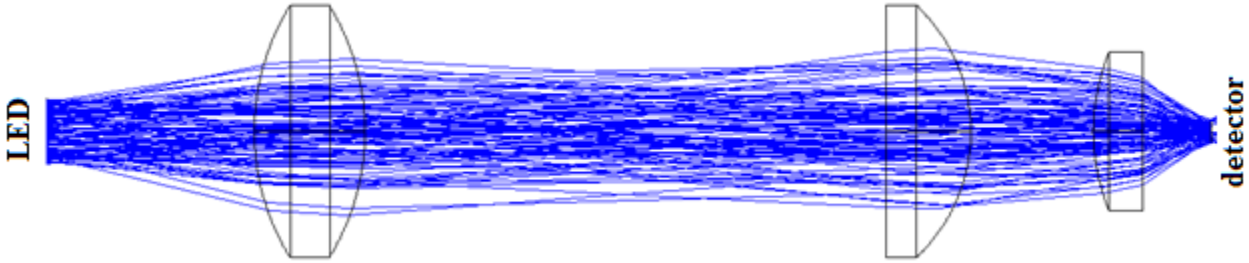

Figure 13: Individual LED evaluation setup simulation.

CHAPTER 5: VALIDATION TESTS

Flow Cell and Setup

For validation and calibration of the absorption sensor, a simple flow cell was constructed out PVC pipe that is shown in figure 14 below. The cell was constructed to facilitate the flow gases with placed inline with its axis to allow access to the sensor. Lenses are placed at each window to collimate the beam for transmission through the cell. A solenoid valve is placed on a T-adapter in line with the air flow. The valve is used to turn the CO/CO_2 mixture on and off and can be cycled at high speeds to create fluctuations in the air flow. This is to evaluate the sensors time resolution.

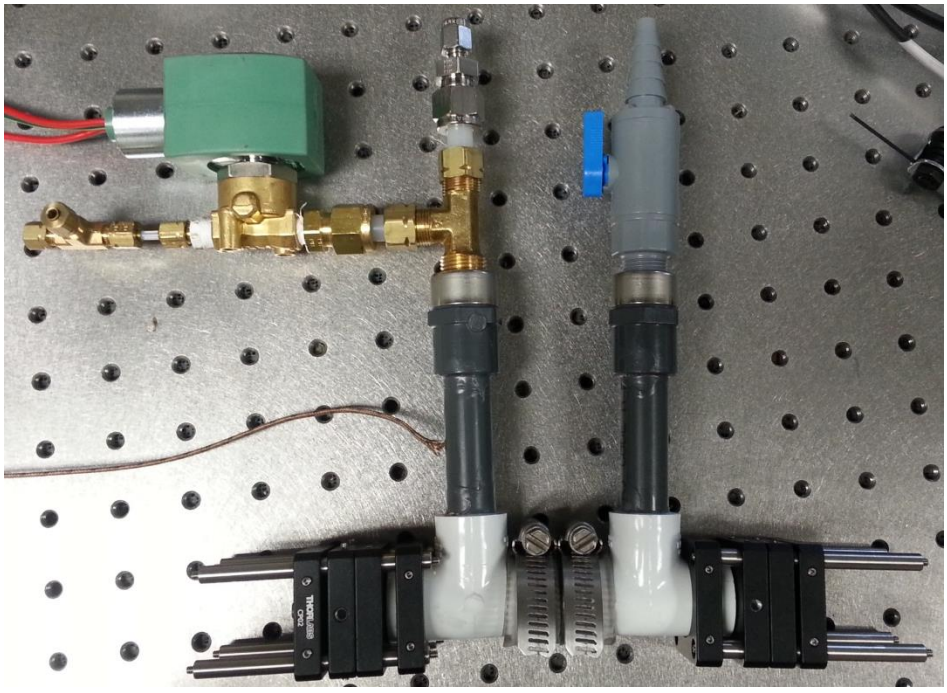

Figure 14: Simple flow cell.

For these evaluation tests the HWG was bypassed and the flow cell was placed directly between the pitch and catch setups. This allowed more tests to be completed with the limited

time available since time did not have to be wasted to properly align the HWG. A tent was placed over the entire setup and purged with synthetic air so to remove trace CO and CO_2 gases. Gas bottles cut with nitrogen (N_2) were used to fill the flow cell with a gas divider used to further dilute the gases so gas concentrations could easily and accurately be stepped through the ranges specified. LEDs at each wavelength were driven with a unique frequency so they can be separated using a FFT. The LED at 3.6μm (reference) was driven at 55kHz, the 4.2μm LED was driven at 77kHz, the two 4.7μm LEDs were driven at 110kHz with 50% duty cycle pulses.

Detectability Limit and Calibration

Evaluation is first done using CO and CO_2 separate in individual tests so the sensor can be calibrated to accurately measure each gas without interference from the other. CO_2 concentrations in synthetic air was stepped from 0 to 1% in steps of 0.1% and then stepped from 0 to 10% in steps of 0.1%. CO concentrations in synthetic air was stepped from 0 to 0.9% in steps of 0.09% and then stepped from 0 to 4% in steps of 0.4%. This process is also used to determine the sensors detectability limit of each gas if measured separately.

Interference Evaluation and Simultaneous Measurements

These test involved holding one gas at a constant concentration while the other is varied so to determine how each gas interferes with the other. The first set of tests involved holding CO_2 at a constant 3% while CO is stepped from 0 to 4% in steps of 0.4%. Additionally, CO and CO_2 are reverse stepped, while CO_2 is stepped from 0 to 10% in steps of 0.1%, CO is stepped from 4 to 0% in steps of 0.4%. Additional test were planned however malfunction equipment prevented this.

CHAPTER 6: RESULTS AND FUTURE WORK

Results

Changes of 0.1% CO_2 was easily detected as shown in figure 15 below. For CO, changes of 0.3% could be detected. The CO measurement were very noisy likely due to the signal being produced by two LEDs, where the other wavelengths were generated using only one LED each. CO also has a tenth of the absorbance that CO_2 has which reduces resolution.

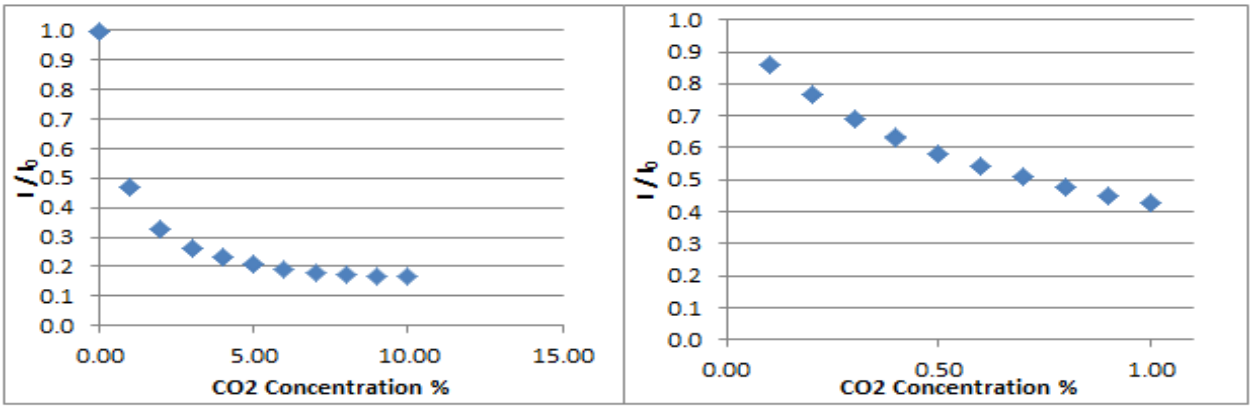

Figure 15: CO2 only measurements vs. the ratio of the transmitted and incident light.

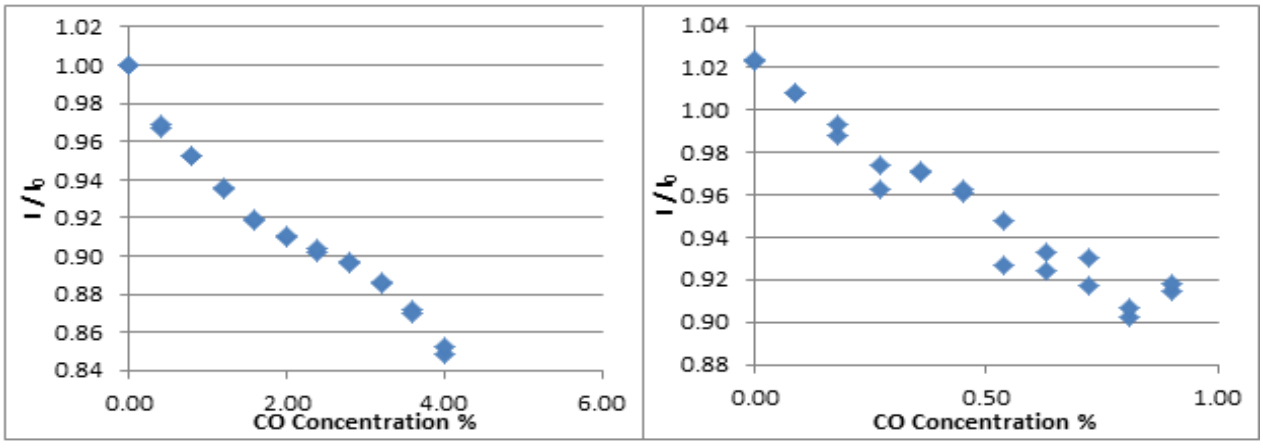

Figure 16: CO only measurements vs. the ratio of the transmitted and incident light.

Figure 17 shows measurements of CO and CO_2, where the CO_2 was held constant and the CO was varied from 0 to 4%. The CO_2 varied no more than 0.2% as the CO was changed which is within the typical standard deviation. Additional tests were perform with varying CO2 and constant CO, however these tests contain bad data and will need to be redone.

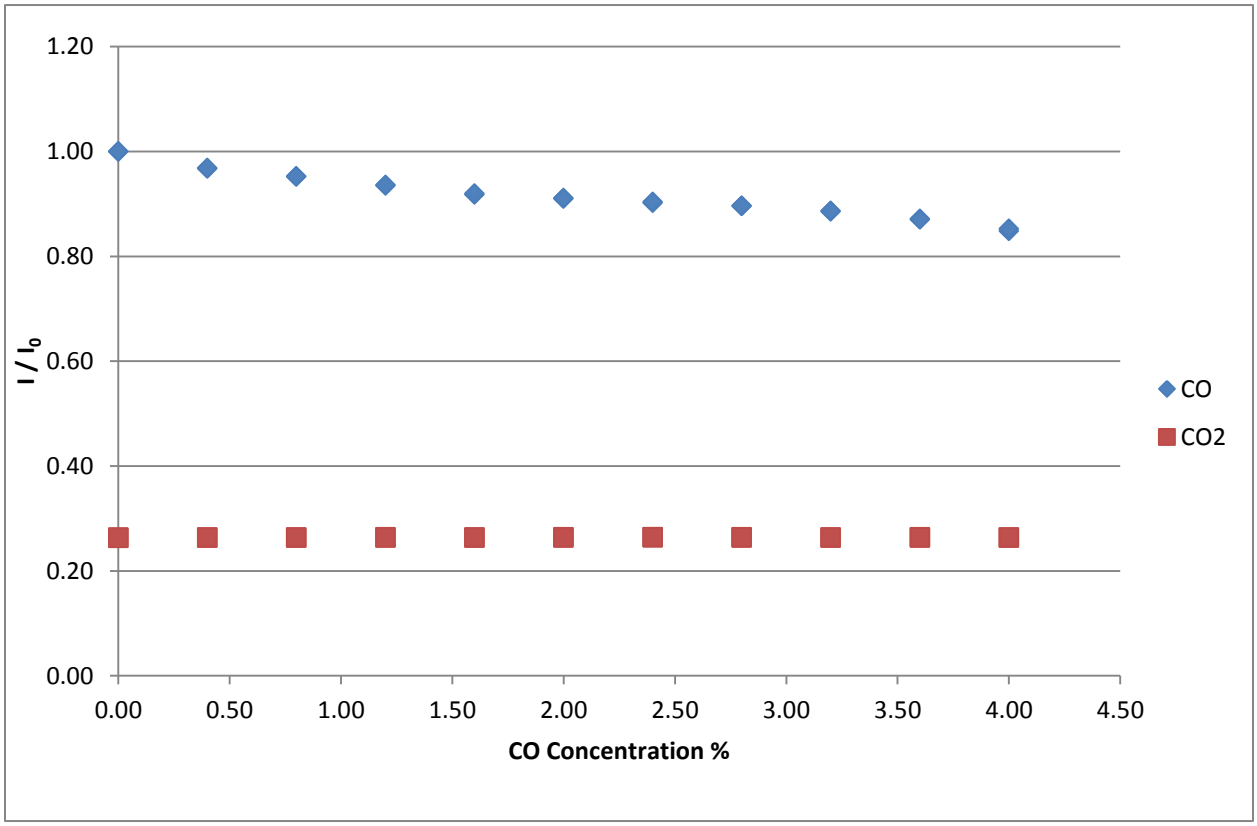

Figure 17: The ratio of transmitted and incident light for simultaneous measurements of constant 3% CO2 with varying CO vs. CO concentration.

The CO measurements were highly inconsistent which may be a result of the signal being generated using two combined LEDs and temperature fluctuations of the LEDs, as well as the low absorbance. All LEDs were cooled to around -15°C however this temperature began to fluctuate after a few hours of testing. This fluctuation could produce instability in the signal and

cause error. Stricter monitoring and control of the LEDs will need to be implemented in future work.

Future Work

Further testing is planned so to fully validate the sensors capabilities. The sensors will be tested using a static cell charged with a known gas composition as well as some interfering species. Additionally, tests will be examining performance in measuring CO and CO_2 in shock-heated nonreactive gases. Finally, the sensor will be validated in a kinetics study of a basic fuel, measuring CO and CO_2 time histories, using a shock tube.

Measurements will be made in a furnace heated, high temperature static cell to demonstrate the sensors functionality at high temperatures and evaluation of interfering species. The cell will be evacuated and charged with a known gas mixture of CO, CO_2, air, and potentially interfering species such as water vapor or fuel. Test mixtures will be manometrically prepared using a high purity, magnetically mixed mixing tank. This will be done for several mixture configurations and temperatures.

Using a stainless steel shock tube, nonreactive gases will be shock heated and evaluated with the sensors. This will allow validation of the sensors performance during dynamic temperature and pressure conditions. The shock tube will be evacuated and loaded with similar gas mixtures as done in the static cell tests. Ren et al. cited the need to add a small portion (%1) of H_2 to the mixture to accelerate CO vibration relaxation [7]. Loading the driver gas with different pressures will produce shock waves of different strengths and temperatures, allowing for a range of conditions.

Finally, the time histories of CO and CO_2 will be monitored in the ignition of a fuel mixture behind a shock wave, using the previously mentioned shock tube. This test will demonstrate the sensors ability to make time-resolved measurements. The fuel mixtures will contain a fuel, O_2, and a diluent and will be prepared manometrically and validated using the mixing facility previously mentioned, equipped with a gas chromatographer. Measurements will be compared to kinetic simulations using CHEMKIN.

The above tests will be conducted using both the laser sensors and the LED sensor with results compared for evaluation of the performance of the LED sensor. This will emphasize the shortcomings of the LED sensor and convey needed design changes to improve performance. These set of tests will also bring greater understanding into strategies for laser absorption spectroscopy and insight into how the LED sensor can be further enhanced.

REFERENCES

[1] 2013, "International Energy Outlook 2013," D. o. Energy, ed.http://www.eia.gov/forecasts/ieo/pdf/0484(2013).pdf.

[2] Manley, D. K., McIlroy, A., and Taatjes, C. A., 2008, "Research needs for future internal combustion engines," Physics Today, 61, pp. 47-52.

[3] Alexander, L., Allen, S., Bindoff, N., Breon, F.-M., Church, J., Cubasch, U., Emori, S., Forster, P., Friedlingstein, P., Gillett, N., Gregory, J., Hartmann, D., Jansen, E., Kirtman, B., Knutti, R., Kanikicharla, K. K., Lemke, P., Marotzke, J., Masson-Delmotte, V., Meehl, G., Mokhov, I., Piao, S., Ramaswamy, V., Randall, D., Rhein, M., Rojas, M., Sabine, C., Shindell, D., Talley, L., Vaughan, D., and Xie, S.-P., 2013, "The IPCC Fifth Assessment Report Climate Change 2013," Intergovernmental Panel on Climate Change, http://www.climatechange2013.org/images/uploads/WGIAR5_WGI-12Doc2b_FinalDraft_All.pdf.

[4] Zheng, M., Reader, G. T., and Hawley, J. G., 2004, "Diesel engine exhaust gas recirculation––a review on advanced and novel concepts," Energy Conversion and Management, 45(6), pp. 883-900.

[5] Reitz, R. D., 2013, "Directions in internal combustion engine research," Combustion and Flame, 160(1), pp. 1-8.

[6] Richards, G. A., McMillian, M. M., and Gemmen, R. S., 2001, "Issues for low-emission, fuel-flexible power systems," Progress in Energy and Combustion Science, 100(3), pp. 312-328.

[7] Ren, W., Farooq, A., Davidson, D. F., and Hanson, R. K., 2012, "CO concentration and temperature sensor for combustion gases using quantum-cascade laser absorption near 4.7 μm," Applied Physics B, 107(3), pp. 849-860.

[8] Farooq, A., Jeffries, J., and Hanson, R. K., 2008, "CO2 concentration and temperature sensor for combustion gases using diode-laser absorption near 2.7 μm," Applied Physics B, 90(3-4), pp. 619-628.

[9] Teichert, H., Fernholz, T., and Ebert, V., 2003, "Simultaneous In Situ Measurement of CO, H2O, and Gas Temperatures in a Full-Sized Coal-Fired Power Plant by Near-Infrared Diode Lasers," Applied Optics, 42(12), pp. 2043-2051.

[10] Mihalcea, R. M., Baer, D. S., and Hanson, R. K., 1998, "Advanced diode laser absorption sensor for in situ combustion measurements of CO2, H2O, and gas temperature," Sumposium (International) on Combustion, 27(1), pp. 95–101.

[11] Schultz, I. A., Goldenstein, C. S., Jeffries, J. B., and Hanson, R. K., 2012, "TDL Absorption Sensor for In Situ Determination of Combustion Progress in Scramjet Ground Testing," Aerodynamic Measurement Technology, Ground Testing, and Flight Testing Conference, 28.

[12] Silver, J. A., 1992, "Frequency-modulation spectroscopy for trace species detection: theory and comparison among experimental methods," Applied Optics, 31(6), pp. 707-717.

[13] Partridge, W. P., Geckler, S., Connatser, M., Yoo, J., Parks, J., Hetisimer, C., and Helman, P., 2011, "Advanced Combustion Engine R&D. Annual Progress Report," Oak Ridge National Lab.

[14] Partridge, W. P., Geckler, S., Yoo, J., Perfetto, A., Parks, J., Connatser, M., Prikhodko, V., and Sanchez-Gonzalez, R., 2012, "Advanced Combustion Engine R&D. Annual Progress Report," Oak Ridge National Lab.

[15] Rothman, L. S., Gordon, I. E., Babikov, Y., Barbe, A., Benner, D. C., Bernath, P. F., Birk, M., Bizzocchi, L., Boudon, V., Brown, L. R., Campargue, A., Chance, K., Cohen, E. A., Coudert, L. H., Devi, V. M., Drouin, B. J., Fayt, A., Flaud, J. M., Gamache, R. R., Harrison, J. J., Hartmann, J. M., Hill, C., Hodges, J. T., Jacquemart, D., Jolly, A., Lamouroux, J., Roy, R. J. L., Li, G., Long, D. A., Lyulin, O. M., Mackie, C. J., Massie, S. T., Mikhailenko, S., Müller, H. S. P., Naumenko, O. V., Nikitin, A. V., Orphal, J., Perevalov, V., Perrin, A., Polovtseva, E. R., Richard, C., Smith, M. A. H., Starikova, E., Sung, K., Tashkun, S., Tennyson, J., Toon, G. C., Tyuterev, V. G., Wagner, G., Müller, H., and Smith, M., 2013, "The HITRAN2012 molecular spectroscopic database," Journal of Quantitative Spectroscopy and Radiative Transfer.

[16] Perry, F., 2013, "IR Detectors from Vigo Systems," Bosten Electronics, http://www.boselec.com/products/documents/-VigoCatalog11-5-13WWW.pdf.

[17] 2013, "Zemax," Radiant Zemax, http://www.radiantzemax.com/en.

APPENDIX: SPECIFICATION SHEETS FOR CRITICAL COMPONENTS

LED36TO8TEC Specifications (3.6μm cooled LED)

Optically Immersed 3.6 µm LED in heat-sink optimized housing			LED36Sr
Peak wavelength	λ_{max}	µm	3.65±0.05
Pulsed power at I=1 A	P_{pulsed}	µW	350±70
CW power at I=200 mA	P_{CW}	µW	135±25
Switching time	τ	ns	≤20

Code	Thread	Emission size, mm	Lens material	Far-field pattern FWHM, deg.	Optical axis deviation, deg	Operation (storage) conditions, °C
LED36Sr	M5×0.5	Ø 3.3	Si	≤20	≤7	-25÷+60 (+80)
LED36TO8TEC			Si lens and quartz window			

Product view

LED36Sr

LED36TO8TEC

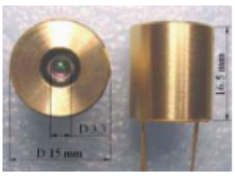

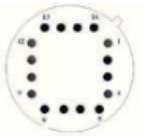

1 TEC –; 4 TEC +
8 LED +; 13 LED –
10, 11 thermosensor

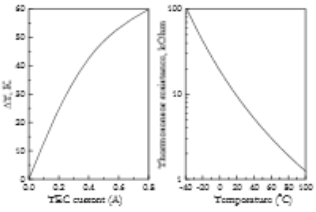

- ✓ All devices are stressed at 80°C (I=0) and I=200 mA (CW, 20°C) for 10 hrs before final test and shipping to a customer.
- ✓ Beam divergence of the LEDs is small and thus we recommend adjusting LED position regarding to the detector system before final evaluation/use of the devices.
- ✓ All data are valid for room temperature (22°C) and LED attached to a heatsink. Heatsink is important for normal LED operation especially in the CW mode.
- ✓ Polarity: see Product view. In near future two color wires will be used.

Output power vs. current, current-voltage curve and emission spectra

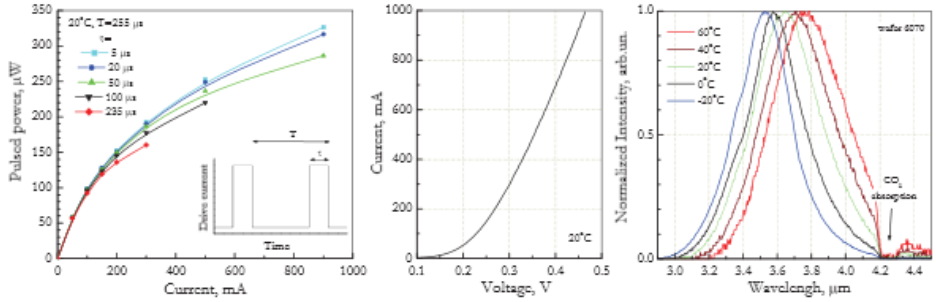

Output power and peak wavelength vs. temperature, far-field pattern and maximal current vs. operation conditions

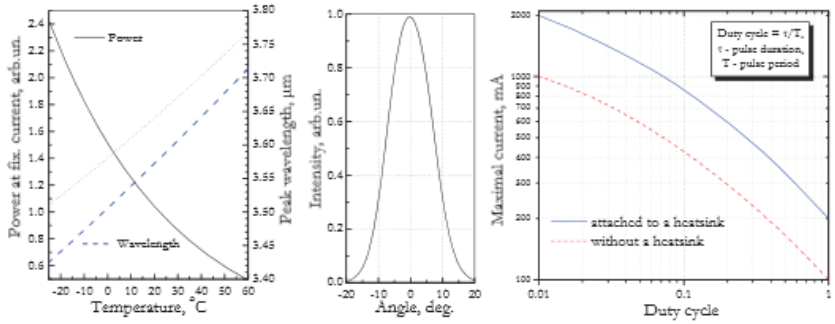

Updated 28.04.09

LED42TO8TEC Specifications (4.2μm cooled LED)

Optically Immersed 4.2 µm LED in heat-sink optimized housing			LED42Sr
Peak wavelength	λ_{max}	µm	4.2±0.1
Pulsed power at I=1 A	P_{pulsed}	µW	70±15
CW power at I=200 mA	P_{CW}	µW	25±5
Switching time	τ	ns	≤20

Code	Thread	Emission size, mm	Lens material	Far-field pattern FWHM, deg.	Optical axis deviation, deg	Operation (storage) conditions, °C
LED42Sr	M5×0.5	Ø 3.3	Si	≤20	≤7	-25÷+60 (+80)
LED42TO8TEC			Si lens and quartz window			

Product view

LED42Sr

LED42TO8TEC

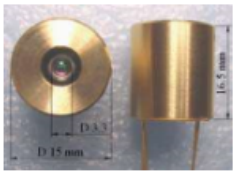

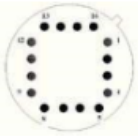

1 TEC –; 4 TEC +
8 LED +; 13 LED –
10, 11 thermosensor

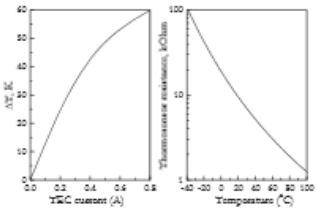

- ✓ All devices are stressed at 80°C (I=0) and I=200 mA (CW, 20°C) for 10 hrs before final test and shipping to a customer.
- ✓ Beam divergence of the LEDs is small and thus we recommend adjusting LED position regarding to the detector system before final evaluation/use of the devices.
- ✓ All data are valid for room temperature (22°C) and LED attached to a heatsink. Heatsink is important for normal LED operation especially in the CW mode.
- ✓ Polarity: see Product view. In near future two color wires will be used.

Output power vs. current, current-voltage curve and emission spectra

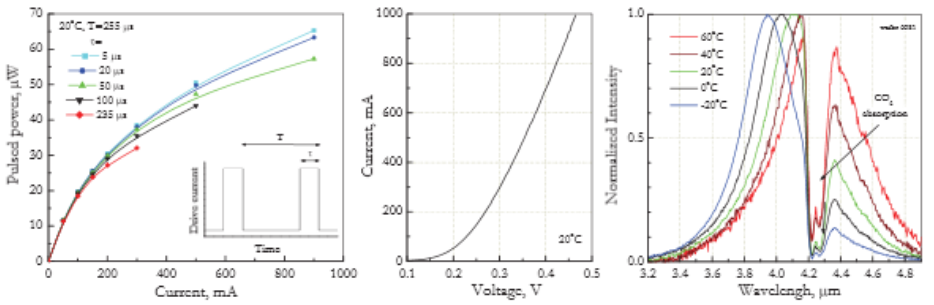

Output power and peak wavelength vs. temperature, far-field pattern and maximal current vs. operation conditions

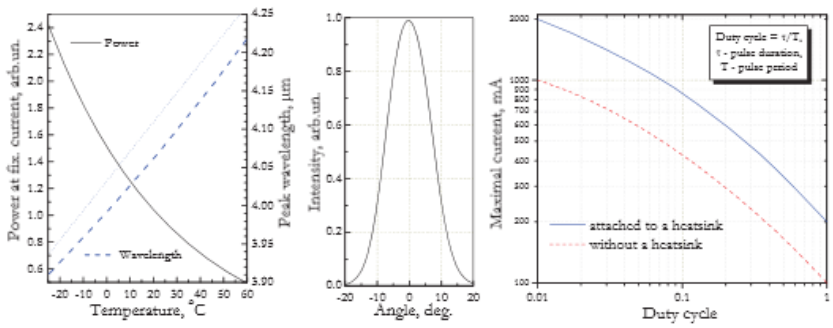

Updated 28.04.09

LED47TO8TEC Specifications (4.7μm cooled LED)

Optically Immersed 4.7 µm LED in heat-sink optimized housing			LED47Sr
Peak wavelength	λ_{max}	µm	4.7±0.05
Pulsed power at I=1 A	P_{pulsed}	µW	25±5
CW power at I=200 mA	P_{CW}	µW	5±1
Switching time	τ	ns	≤20

Code	Thread	Emission size, mm	Lens material	Far-field pattern FWHM, deg.	Optical axis deviation, deg	Operation (storage) conditions, °C
LED47Sr	M5×0.5	Ø 3.3	Si	≤20	≤7	-25÷+60 (+80)
LED47TO8TEC			Si lens and sapphire window			

Product view

LED47Sr

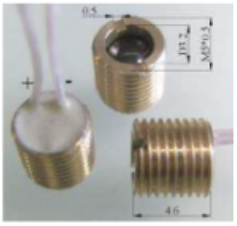

LED47TO8TEC

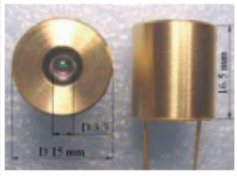

1 TEC −; 4 TEC + 8 LED +; 13 LED − 10, 11 thermosensor

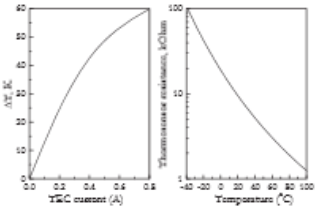

- ✓ All devices are stressed at 80°C (I=0) and I=150 mA (CW, 20°C) for 10 hrs before final test and shipping to a customer.
- ✓ Beam divergence of the LEDs is small and thus we recommend adjusting LED position regarding to the detector system before final evaluation/use of the devices.
- ✓ All data are valid for room temperature (22°C) and LED attached to a heatsink. Heatsink is important for normal LED operation especially in the CW mode.
- ✓ Polarity: see Product view. In near future two color wires will be used.

Output power vs. current, current-voltage curve and emission spectra

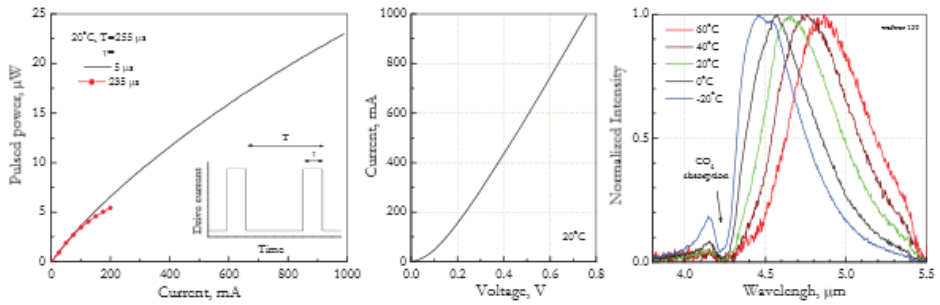

Output power and peak wavelength vs. temperature, far-field pattern and maximal current vs. operation conditions

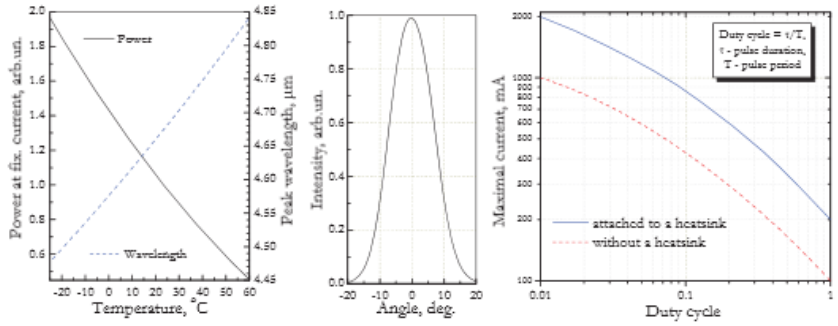

Updated 28.04.09

PVI-3TE Photovoltaic Detector Specifications

PVI-3TE SERIES

2-12 µm IR PHOTOVOLTAIC DETECTORS THERMOELECTRICALLY COOLED OPTICALLY IMMERSED

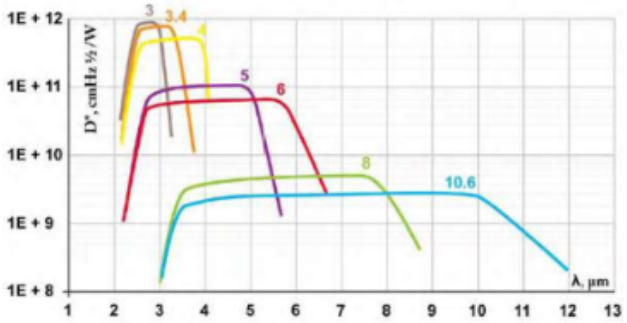

FEATURES

- High performance in the 2-12 µm wavelength range
- Fast response
- No flicker noise
- Convenient to use
- Wide dynamic range
- Compact, rugged and reliable
- Low cost
- Prompt delivery
- Custom design upon request

DESCRIPTION

PVI-3TE-λ_{opt} photodetectors series (λ_{opt} - optimal wavelength in micrometers) feature 3-stage thermoelectric cooler IR photovoltaic detector, optically immersed to high refractive index GaAs hyperhemispherical (standard) or hemispherical or any intermediate lens for different acceptance angle and saturation level. The devices are optimized for the maximum performance at λ_{opt}. Cut-on wavelength can be optimized upon request. Reverse bias may significantly increase speed of response and dynamic range. It results also in improved performance at high frequencies, but 1/f noise that appears in biased devices may reduce performance at low frequencies. Highest performance and stability are achieved by application of variable gap (HgCd)Te semiconductor, optimized doping. Standard detectors are available in TO-8 packages with BaF2 windows. Other packages, windows and connectors are also available.

SPECIFICATION

@20°C

CHARACTERISTICS	UNITS	PVI-3TE-3	PVI-3TE-3.4	PVI-3TE-4	PVI-3TE-5	PVI-3TE-6	PVI-3TE-8	PVI-3TE-10.6
λ_{opt}	µm	3	3.4	4	5	6	8	10.6
Detectivity[1]:	cmHz$^{1/2}$/W							
@ λ_{peak}		≥9×10^{11}	≥7×10^{11}	≥5×10^{11}	≥1×10^{11}	≥6×10^{10}	≥5×10^{9}	≥3×10^{9}
@ λ_{opt}		≥7×10^{11}	≥5×10^{11}	≥3×10^{11}	≥8×10^{10}	≥3×10^{10}	≥3×10^{9}	≥1.5×10^{9}
Responsivity @ λ_{opt}	A/W	≥0.5	≥0.8	≥1	≥1.3	≥1.5	≥1	≥0.7
Time constant	ns	≤20	≤20	≤20	≤20	≤15	≤8	≤6
Resistance-optical area product	Ω×cm^2	≥24000	≥1500	≥600	≥30	≥2.5	≥0.04	≥0.02
Operating temperature	K	~210						
Acceptance angle, F/#	deg, -	36, 1.62						

[1] Data sheet states minimum guaranteed D* values for each detector model. Higher performance detectors can be provided upon request.

[2] Faster response may be achieved with high-frequency-optimized devices.

Type	Length or diameter [mm]								
	0.025	0.05	0.1	0.2	0.25	0.5	1	2	3	4
PVI-3TE-3					O	X	X	O		
PVI-3TE-3.4					O	X	X	O		
PVI-3TE-4					O	X	X	O		
PVI-3TE-5					O	X	X	O		
PVI-3TE-6					O	X	X	O		
PVI-3TE-8				X	X	X[1]	P			
PVI-3TE-10.6				X	X	X[1]	P			

[1] Custom detector may require reverse bias in order to increase dynamic resistance and improve frequency response.

X – standard detectors
P – default with reverse bias
O – detectors available on request, parameters may differ from these in data sheets

Warsaw Poland; e-mail: info@vigo.com.pl Agent: Boston Electronics, Brookline MA USA +1 617 566 3821; vigo@boselec.com